2009 年臺灣國際科學展覽會

優勝作品專輯

編號： **140024**

作品名稱

凌波仙子—水黽蓮花效應的實驗與探討

得獎獎項

物理與太空科學科大會獎第三名

學校名稱： 國立臺南女子高級中學

作者姓名： 曾培琪　林睿涵

指導老師： 林仁輝　黃哲男

關 鍵 字： **lotus effect, contact angle, strider**

作者簡介

我是曾培琪，今年就讀台南女中二年級。從小興趣廣泛，科學、音樂、體育、語文、童軍、國際事務等均有所涉獵。目前在學校活躍的參與各類活動，並且是排球隊的一員。從國小開始接觸科學實驗與研究，平常亦喜歡閱讀科普相關雜誌與文章。和林睿涵是認識多年的鄰居兼同學，高一下開始在採蓮花以及捕水黽。這次的研究過程讓我學到很多，也是人生寶貴的經驗。

我是林睿涵，目前就讀台南女中二年級，平時喜歡看書、運動、聽別人說科學。目前是學校籃球隊的隊員。偶然的機會下參加這次科展，讓我能夠動手做科學，並學習更多從沒接觸過的事物、培養科學精神。希望未來我能繼續參與相關研究，更深入的了解其中的奧妙。

凌波仙子—水黽之蓮花效應的實驗與探討

摘要

本報告分為兩個部份：理論與實驗。在理論部份，我們推導出一個可以計算規則表面接觸角方程式，並建立一個水珠停留在粗糙表面上所造成之水橋的模型，求出方程式中的未知數，即可求出接觸角。

在實驗部份，我們利用新的量測方法測量水黽腳在入水至離開水面時所受的鉛直力和水平力。此實驗分別在靜止水面、搖晃的水面、以及流動的水面上進行。在各個實驗中所量測到的力都小於 50 微牛頓，是相當小的。這微小的力量來自於水黽腳超疏水的特性，而也加強了水黽腳的抗震與抗摩擦功能。另外，我們也得知固體的潤濕度對於接觸角和黏附力都有影響。

Theoretical and Experimental Studies of Lotus Effect Occurring at a Strider on Water Surface

Abstract

This study aims to unveil the hydrophobic characteristic of the lotus effect by investigating the hydrophobicity of the nanostructures of the lotus leaf and conducting experiments by using the strider leg.

The study consists of two parts, the theoretical analysis and the experimental tests. In the theoretical part, our research showed that the hydrophobicity of nanostructures is determined by the contact angle formed between the water droplet and the rough surface.Then, an equation was developed to further calculate the actual contact angle on a rough surface. With the establishment of a new model that can be used to determine the stagnant position of the water droplet, functions in the equation are thus obtained to calculate the actual contact angle.

In the experimental part, the vertical and horizontal forces of the strider leg treading on calm, vibrating and flowing water surfaces are measured with a new method. All the measured forces are below 50μN, which is considerably minimal. These small forces are due to the effects of the hydrophocity of the strider leg. They also displayed the strider leg's antifriction and antivibration, which enabled the strider to stride on the water surface. The strider leg's setae are found to account for the leg's hydrophobicity. The setae are analyzed by employing the developed theoretical model to find a contact angle of 123.5°. The combination of many setae results in a contact angle of over 170° on water for the strider leg. We have also confirmed that the wettability of the material affects the contact angle and drag force.

Theoretical and Experimental Studies of Lotus Effect Occurring at a Strider on Water Surface

1. Introduction

The lotus effect is now a well-known phenomenon in the world of nature. However, we understand that the lotus effect is a feature that belongs not only to the lotus leaf but also to other plants and even some animals as well. Besides, many characteristics of the lotus effect remain unknown. How do the complicated nanostructures affect the hydrophobicity of the materials? How do striders “stride” on the water surface? These are just some of the mysteries that have inspired our curiosity and motivated us to dwell further into the world of the contact angle, hydrophobicity, and the lotus effect.

2. Objectives

2.1 To examine different surface structures in nature and their hydrophobicity, and understand how the different arrangements of the surface structures affect the contact angle, and thus the hydrophobicity of the material. Establish an equation that can show the relationship between the contacting condition of the materials and the contact angle.

2.2 To study the hydrophobicity and characteristics of materials with small physical structure in liquids of different properties. Measure the forces of a strider and other materials treading on water, and conduct experiments on moving water.

3. Theoretical Analysis

The profile of the water droplet formed on a surface are determined by the roughness and the nanostructures of the material surface. The physical representation of this phenomenon is defined by the contact angle. The bigger the contact angle is, the better the hydrophobicity of the material. The lotus effect occurs when the material is of high hydrophobicity. The contact angle is believed to be controlled by the chemical compositions of the material and the physical structure of the surface. The effect of the surface microstructure on the contact angle is discussed below.

3.1 Models for Determining Actual Contact Angle

Hydrophobicity is often determined by the contact angle. The contact angle of a droplet of constant volume on a solid surface without roughness is represented by Young's equation(1):

$$\cos\theta_0 = (\gamma_s - \gamma_{ls}) / \gamma_l , \tag{1}$$

where γ_s, γ_l, and γ_{ls} represent the interface energies between solid-vapor, liquid-vapor, and liquid-solid, respectively (Figure 1.).

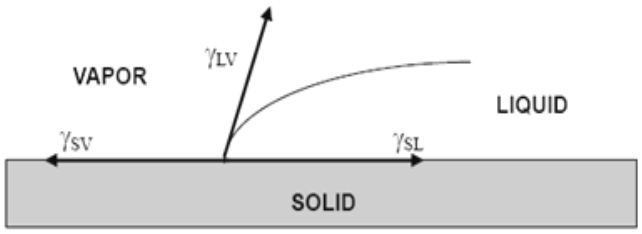

Figure 1. Schematic diagram of three interface energies formed on a smooth surface.

However, Young's equation does not equitably manifest the actual contact angle formed on a rough surface. Therefore, the models with rough surfaces was introduced. In Wendel's theory(2), the grooves of the rough surface are entirely filled by the liquid, resulting in a fully wetted formation (see Figure 2.a). The contact angle with this rough surface is defined as:

$$\cos\theta = D\cos\theta_0, \tag{2}$$

where D, as shown in Figure 3., is the roughness parameter which is defined as the average ratio of the real attached interface (wetted area, S_1) to its projection area on the horizontal plane (S_1'); therefore $D = S_1 / S_1'$. θ_0 is the contact angle of the material assuming without surface roughness; whileas the θ angle is the real contact angle of the material, taking the surface roughness into consideration. In the approach of the Cassie and Baxter(3), it assumed that the liquid left out of the grooves completely, thus creating a composite formation. The contact angle produced by this model can be expressed as:

$$\cos\theta = (1-F)\cos\theta_0 - F, \tag{3}$$

where F denotes the area fraction of non-contact solid-liquid interface (S_2') on the projection area (S_0) of the solid-liquid contacts (see Figure 3.). Therefore,

$$F = S_2' / S_0.$$

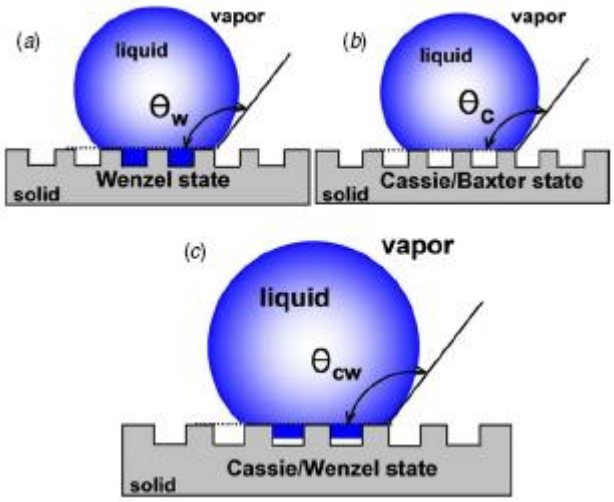

Figure 2. The three models of liquid on rough surfaces.

3.2 Water Bridge Profile

But the models mentioned above are still unrealistic. In the real state with the liquid-solid interface, the liquid neither fills the grooves completely; nor is it entirely excluded from the grooves. In fact, the liquid is partly entrapped way in the grooves, thus developing a water bridge suspended at a certain height of the groove. Therefore, a new state is developed in the present study to simulate the situation (Figure 2.c). The contact angle of the new state is analyzed below.

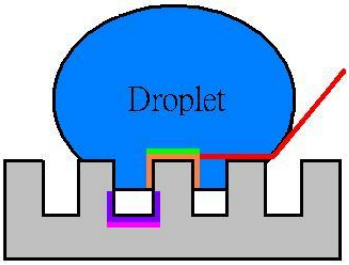

Figure 3. The condition of the droplet contacting rough surface.

Note: orange: S_1 green: S_1' purple: S_2 pink: S_2'

According to the study of Zhou and Hosson, the interface of the liquid and air can be considered with the aid of the minimum energy condition. G is the radius of the spherical liquid droplet and H is the height of the droplet center measured from the solid surface. The surface area of the liquid droplet is given as $S_L = 2\pi G(G+H)$ and the projection area of the rough solid surface on the horizontal plane is $S_0 = \pi(G^2 - H^2)$. The interface area of wetted parts is S_1 and that of unwetted parts is S_2. The projection areas of S_1 and S_2 on the interface S_0 are S_1' and S_2', respectively, so $S_1' + S_2' = S_0$. Thus, D is the roughness parameter of Wenzel's type(4) and F is that of Cassie and Baxter's type. Obviously $D > 1$ and $F < 1$. The total energy after the contact of the liquid and solid surface can be expressed as:

$$\begin{aligned} E &= \gamma_l S_L + \gamma_l S_2' + (\gamma_{ls} - \gamma_s) S_1 \\ &= \gamma_l S_L + \gamma_l F S_0 + (\gamma_{ls} - \gamma_s) D S_1' . \end{aligned} \tag{4}$$

and

$$S_1' = S_0 - S_2' = S_0 - F S_0 = S_0(1-F) . \tag{5}$$

The real contact angle θ can be taken from the geometrical image of the sphere droplet, so $\cos\theta = -H/G$. H and G are two functions of θ. The total energy can be expressed by the following formula:

$$\begin{aligned} E &= \gamma_l 2\pi G(G+H) + \gamma_l F \pi (G^2 - H^2) + (\gamma_{ls} - \gamma_s) D(1-F)\pi (G^2 - H^2) \\ &= \pi\gamma_l \left\{ 2G(G+H) + (G^2 - H^2)\left[F + D(1-F)\frac{\gamma_{ls} - \gamma_s}{\gamma_l} \right] \right\} \\ &= \pi\gamma_l \left\{ 2G(G+H) + (G^2 - H^2)\left[F - D(1-F)\cos\theta_0 \right] \right\} \\ &= \pi\gamma_l G^2 \left[2 + 2\frac{H}{G} + \left(1 - \left(\frac{H}{G} \right)^2 \right)\left(F - D(1-F)\cos\theta_0 \right) \right] \\ &= \pi\gamma_l G^2 \left[2 - 2\cos\theta + \left(F - D(1-F)\cos\theta_0 \right)\sin^2\theta \right]. \end{aligned} \tag{6}$$

Then, it is known that the minimum energy condition satisfies $dE/d\theta = 0$ in the complete system. This can be applied to Eq.(6), which results in the following equation:

$$-2\frac{dG}{d\theta}\left(2-2\cos\theta+A\sin^2\theta\right)=G\left(2\sin\theta+2A\sin\theta\cos\theta\right). \tag{7}$$

where $A=F-D(1-F)\cos\theta_0$. From the experimental results, the average volume of droplets was about $5\times10^{-9}m^3$ (the diameter of a spherical droplet was about $2.1\times10^{-3}m$). According to numerical calculations, the volume of the liquid in the groove is approximately $10^{-13}m^3$. So, the volume of the liquid in the groove is comparatively small to the whole droplet, thus the volume of the liquid in the grooves does not significantly effect the contact angle. The spherical droplet volume can be expresses as:

$$\begin{aligned} V &\cong \frac{1}{3}\pi(G+H)^2(3G-(G+H)) \\ &=\frac{1}{3}\pi G^3\left(1+\frac{H}{G}\right)^2\left(2-\frac{H}{G}\right) \\ &=\frac{1}{3}\pi G^3(1-\cos\theta)^2(2+\cos\theta) \\ &=Constant. \end{aligned} \tag{8}$$

The constant liquid droplet volume satisfies the condition:

$$\begin{aligned} \frac{dV}{d\theta} &= \frac{1}{3}\pi 3G^2\frac{dG}{d\theta}(1-\cos\theta)^2(2+\cos\theta) \\ &\quad+\frac{1}{3}\pi G^3 2(1-\cos\theta)(\sin\theta)(2+\cos\theta) \\ &\quad+\frac{1}{3}\pi G^3(1-\cos\theta)^2(-\sin\theta)=0. \end{aligned} \tag{9}$$

The above equation is rearranged as:

$$-\frac{dG}{d\theta}=\frac{G(1+\cos\theta)\sin\theta}{(2+\cos\theta)(1-\cos\theta)}. \tag{10}$$

Substituting Eq. (10) into Eq. (7) gives:

$$-2\cos^2\theta+(2-2A)\cos\theta+2A=0. \tag{11}$$

The solution of $\cos\theta$ gives as:

$$\cos\theta=D(1-F)\cos\theta_0-F. \tag{12}$$

If $F=0$, Eq.(12) reduces to Wenzel's equation; and if $D=1$, Eq.(12) becomes Cassie and Baxter's formula. The solutions of D and F are obtained using the following method.

If the grooves at the solid body is of perfect square wave form, the condition of the liquid in the grooves are either at the Wenzel state or the Cassie and Baxter state. However, perfect square wave forms of surfaces are rare in the nature; most of the natural materials tend to be closer to a circular wave form, which may vary widely because of different radii of the curvature. In order to express the square wave model with round corners, finite terms of the Fourier series are used. If only partial parts of the Fourier series are used to make up the model, the lateral surfaces of the groove become curved. In this way, the walls of the grooves are no longer perpendicular to the horizon, even if many terms are adopted in the Fourier series to describe the groove profile. The liquid can be considered to be entrapped inside the grooves, where a stagnant water bridge is formed, and suspended somewhere in the groove. In the current studies, a numerical method is developed to find the stagnant point and the suspended profile of the water bridge.

In order to determine the hydrophobicity of the system, the Fourier series are used to simulate various geometrical shapes. If the system is cyclically grooved, the surface of the system, z(x), can then be described with a sinusoidal function z_i with angular frequency w_i as:

$$z(x) = \sum_{i=0}^{\infty} z_i(x) = \sum_{i=0}^{\infty} a_i \cdot \cos(\omega_i \cdot x) \quad . \tag{13}$$

Since the data of $z(x)$ resampled discretely by a profilometer, the frequency w is in influenced greatly by the measured length L and the sampling interval l_s of two adjacent data points. The range of frequency varies from the lower bound of $f_l = \omega_l / (2 \cdot \pi) = 1/L$ to the upper bound of $f_h = \omega_h / (2 \cdot \pi) = 1/(2 \cdot l_s)$; i.e. the Nyquist frequency. The topography of the square wave is considered to be composed of numerous sinusoidal profiles with different radii of curvature at the summit. Different geometries can thus be created using the first several partial terms of the corresponding Fourier series. In present study, the water is believed to be stagnant at a certain point on the lateral surfaces of a groove. The stagnant point on the lateral surface and the profile of the water bridge remains unknown. In order to determine the existence of the water bridge, Eq. (13) is differentiated w.r.t. x as $x \neq 0$:

$$z'(x) = -\sum_{i=0}^{\infty} a_i \cdot \omega_i \cdot \sin(\omega_i \cdot x) \quad . \tag{14}$$

The system is considered to be two-dimensional. Two arbitrary points on the lateral surface, A and B, can therefore be expressed as ($x_A, z_A(x)$) and ($x_B, z_B(x)$) (Figure 4.). From Eq. (14), the slopes of point A and point B are:

$$m_1 = z'(x_A); \quad m_2 = z'(x_B) \quad . \tag{15}$$

The tangents of the groove at the two points A and B are two straight lines

with the slopes of m_1 and m_2 respectively. The original contact angle θ_0 can be obtained from contact angle measurements if the liquid droplets and the solid material are available. Then, two lines with the slopes of m_3 and m_4 ,as shown in Figure 4., is obtained by slanting the line with the slope of m_1 leftward by θ_0, and slanting the line with the slope of m_2 rightward by θ_0 too. The slopes of these two lines, denoted as m_3 and m_4 can be expressed as:

$$\begin{aligned} m_3 &= (-1+\tan\theta_0 \times m_1)/(\tan\theta_0 + m_1); \\ m_4 &= (-1+\tan\theta_0 \times m_2)/(\tan\theta_0 + m_2). \end{aligned} \tag{16}$$

Two lines perpendicular to the line with slopes of m_3 and m_4, and passes through the points A and B intersect at point O. The slopes of the two lines $\overline{OA}$ and $\overline{OB}$, are obtained as:

$$\begin{aligned} m_{OA} &= -\frac{1}{m_3}; \\ m_{OB} &= -\frac{1}{m_4}. \end{aligned} \tag{17}$$

The coordinates of this intersection point O are expressed as:

$$\begin{aligned} x_0 &= (z_2 - z_1 + m_2 x_1 - m_4 x_2)/(m_2 - m_4); \\ z_0 &= (m_4 z_1 - m_2 z_2 + m_2 m_4 x_2 - m_2 m_4 x_1)/(m_4 - m_2). \end{aligned} \tag{18}$$

Then, lengths of $\overline{OA}$ and $\overline{OB}$ are written as:

$$\begin{aligned} \overline{OA} &= \sqrt{(x_1 - x_0)^2 + (z_1 - z_0)^2}; \\ \overline{OB} &= \sqrt{(x_2 - x_0)^2 + (z_2 - z_0)^2}. \end{aligned} \tag{19}$$

The round profile of the liquid at the groove exists only when $\overline{OA}$ is equal to

$\overline{OB}$. If $\overline{OA} \neq \overline{OB}$, other choices of A and B points on the two lateral surfaces of this groove should be automatically selected by the computer until the $\overline{OA} = \overline{OB}$ condition is satisfied. If no such set of points on these two lateral surfaces can be found the water droplet is operating at either the Wenzel condition or the Cassie and Baxter condition. It should be mentioned that several pairs of points may satisfy the condition $\overline{OA} = \overline{OB}$. However, the existence of a round profile is valid for the area of this profile having the minimum length of these round profiles, because this way the system can maintain a minimum energy.

After the stagnant point and the profile of the water bridge have been determined, the D and F can be calculated and thus used in the Eq.(11) to find the real contact angle of a rough surface.

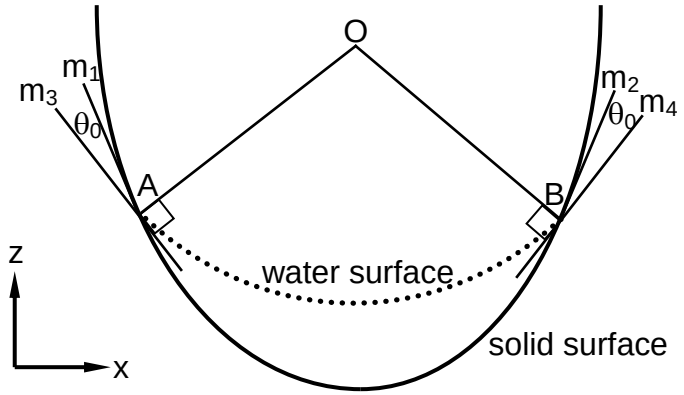

Figure 5. The scheme used to determine the water-bridge stagnant condition.

4. Experimental Studies on Vertical and Horizontal Forces of Strider Leg at Different Water Operating Conditions

4.1 Equipments and devices required in experimental studies

(1) Microscopes: AFM, SEM

(2) Contact angle goniometer

(3) Nano Indenter

(4) Plastic tubes and glass tubes

(5) Miniature water pump

(6) CCD camera system

(7) Sponge

4.2 Examination of the Nanostructures with Lotus Effect

4.2.1 Examination of the nanostructure of the lotus leaf

Samples of the lotus leaf (Nelumbo nucifera) were cut at a size of around 2 cm× 2 cm, and attached onto the slides and examined for surface roughness under the AFM and SEM. Data of surface roughness were recorded. A contact angle goniometer (MagicDroplet Model 100) was then applied to measure the contact angle of the leaf samples.

4.2.2 Examinations of the Nanostructures of the Roach and the Strider Legs

Specimens of the middle legs of a cockroach (Periplaneta americana) and a strider (Gerris remigis) were taken from creature bodies and then examined using an optical microscope with a magification of 10, 40, 100, and 400 times

respectively. Photographs of the specimens were then used to calculate the sizes and distribution of the setae.

4.3 Adhesive Force Measurements during Water Treading

4.3.1 The Self-Developed System for Adhesive Force Measurements

In order to simulate the adhesive force of the leg actions at water treading against the water surface and photograph the entire process, a new system, as shown schematically in Figure 6., was developed to be the combinations of follwing three different apparatuses:

(a) TriboScope system (Hysitron, US) (Figure 7.) was used to measure the force of treading against water. The sample was first attached to the transducer of the TriboScope system, which was then turned to the open-loop mode. The measured force of the system is adjusted to be zero when the sample is suspended far away from the water surface by compromising the weight of the indenter column with the sample. The resulting force of the sample is thus balanced during the whole process.

(b) The stage of the SPM scanning probe microscope (Seiko, Japan) was used to elevate and vibrate horizontally the water vessel. The water vessel could be moved vertically at a constant speed, with the highest speed at 33 μm/s and the lowest speed at 16 μm/s, and horizontally at a frequency of 5, 10, 50 Hz respectively, with an amplitude of 2 mm.

(c) The CCD camera system: optical lenses and a CCD camera system were applied to photograph record the film at 30 frames/s.

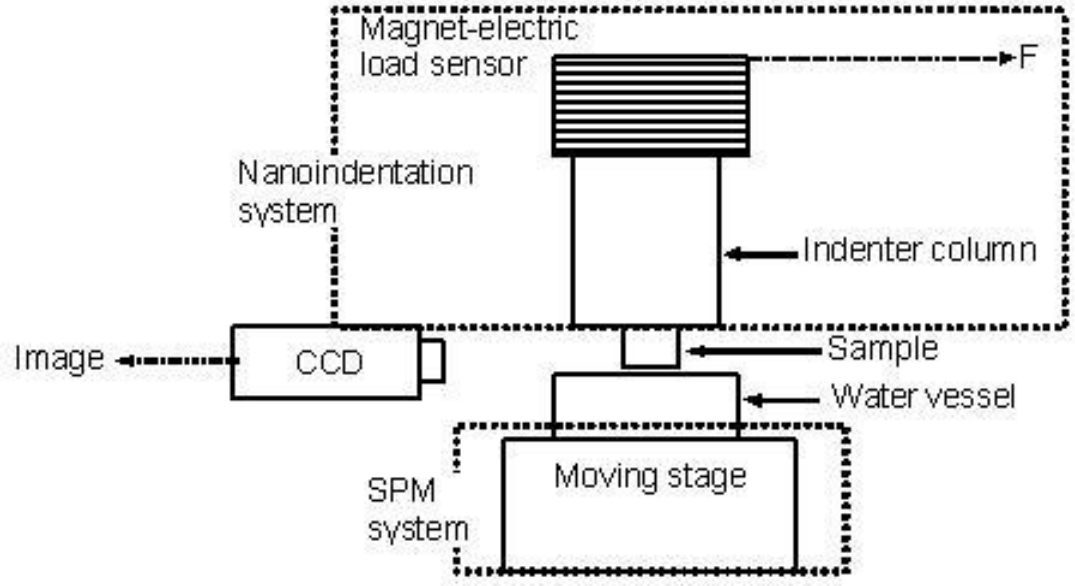

Figure 6. Newly developed-system for measuring adhesion forces, it is composed of the stage of the SEM, the TriboScope system, and a CCD camera set.

Figure 7. The combined system of an AFM and a nanotester for forces measurements in two directions.

4.3.2 The Pilot Study for the Measurement of Adhesive Force during Water Treading

For the purpose of examining the of the effect of adhesive force on the water treading, a pilot study was conducted by using a punch in place of the specimen and a water droplet in place of the water surface. The water droplet was placed on the stage which was controlled by a computer to simulate the five steps of water treading: the water droplet got into contact with the punch, then the stage continued to elevate; it paused for a while, and then lowered, finally left the punch. Measurements of adhesive force were made simultaneously.

4.3.3 Definitions of Terminology for the Five Steps of Water Treading

To facilitate the understanding of the five steps of water treading, the following terminologies are used to denote the five steps of the water treading procedure, which lasted less than 1/30 second.

(a) Jump-into-Contact: the point at which the punch got into contact with the droplet.

(b) Loading: the process in which the punch dipped into the water droplet after the jump-into-contact point.

(c) Dwelling: the brief time at which the stage was paused.

(d) Unloading: the retreat of the water droplet before it completely left the punch.

(e) Jump-off-Contact: the point at which the punch lost contact with the water droplet.

The above procedures apply to all of the water treading experiments below, and the presentations and discussion of the results are shown in Sec. 5 of this study.

4.3.4 The Vertical Force Measurements during Treading on Calm Water

The treading was controlled by lifting the water vessel when the water surface got into contact with the specimen, then continued to elevate this vessel so that the specimen dipped into the water, dwelled briefly, then conducted the unloading, and finally lost contact with the water surface when jump-off-contact occured.

4.3.5 The Vertical and Horizontal Forces Measured during the Treading on Vibrating Water Surface

The water vessel was first moved to get into contact with the specimen, and then vibrating with the specimen dipped into the water, then conducted the unloading; and finally, the water surface lost contact with the specimen.

4.3.6 The Vertical and Horizontal Forces during the Treading on Flowing Water

This experiment was conducted by replacing the original water vessel with a specially-made glass tube which is 20 cm in length and 3 cm in depth. A rectangular hole was given in the middle of the glass tube, such that it provided the sample to be dippled into the water flow at different depths. This specimen was held by the cantilever connected with the transducer of the TriboScopeSystem. This rig was horizontally placed on the stage during the testing process. The vertical and horizontal forces were thus measured when the water flowed around the strider leg. Water circulated in the tube continuously by a pump to create a constant water flow (Figure 8.). The water level (which is also used to determine the flow velocity) was controlled by a valve attached at the circulating tubes. The stage was controlled in the same process as shown in

Sec. 4.3.1. In order to achieve a smooth water surface of the flow, a sponge was installed at the entrance of the glass tube.

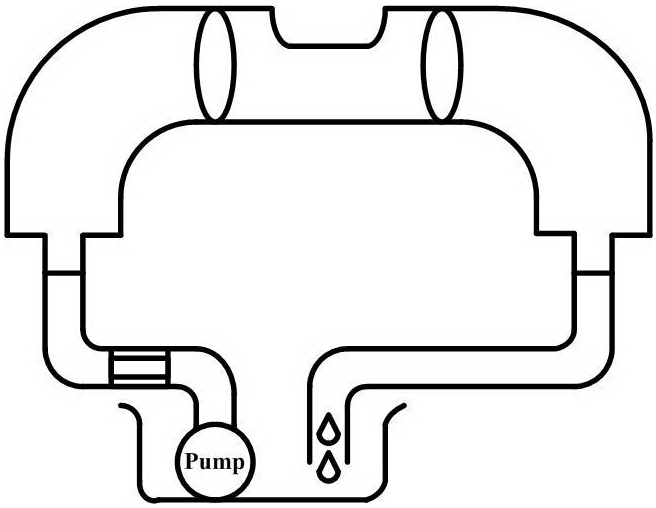

Figure 8. The self-designed glass tube for water slow circulation.

5. Results and Discussion

5.1Nanostructures of the Bio-Specimens

5.1.1 Nanostructures of the Lotus Leaf

The surface of the lotus leaf has wildly scattered asperities, which are covered with wax-like material (Figure 9.). Each of the asperities is unique in size and shape. The morphology and data of the nanostructure of the lotus surface were taken by the AFM (Figure 10.), and put into the MatLab software to simulate using polynomial and the Fourier series. However, the power of the nature wonders proved to be too marvelous to be reproduced.

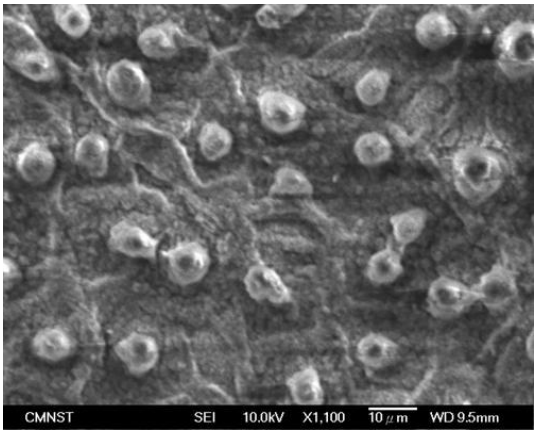

Figure 9. Surface asperities of a lotus leaf under scanned under SEM.

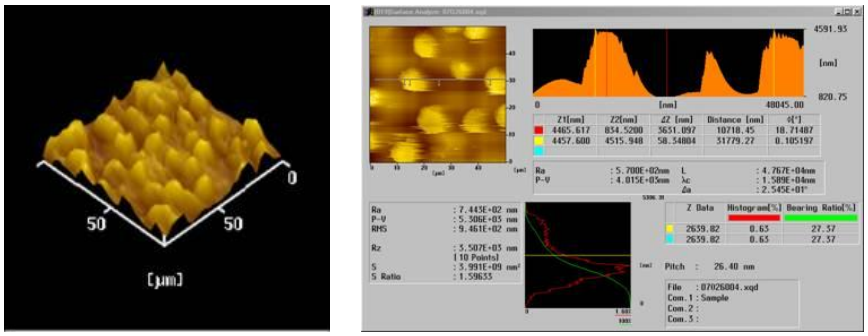

Figure 10. Surface profile of the lotus leaf, and data obtained from the use of an AFM.

5.1.2 Nanostructures of the Cockroach and Strider Legs

As we know, the strider is able to float and move swiftly on the water surface while the roach sinks as soon as it reaches the water. Under the microscope, the strider leg (Figure 11.a) surface is studded with microstructures of the setae coated with wax coverings. The roach legs (Figure 11.b) also have setae; however, its setae are larger in size and are wider in spacing between any two adjacent ones compared to that of the strider.

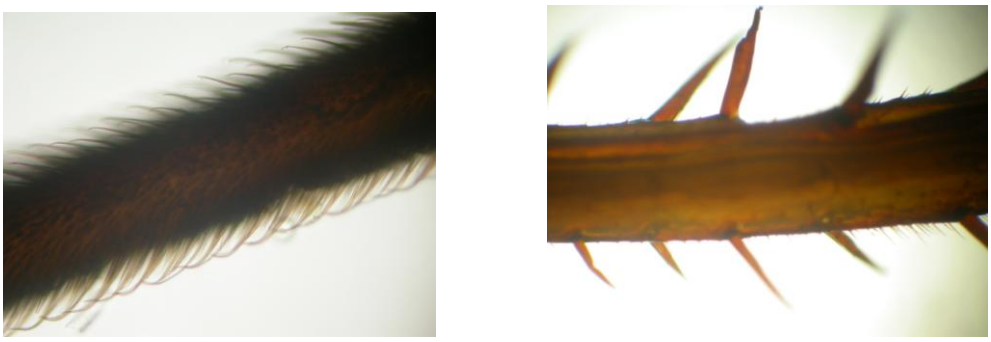

(a) (b)

Figure 11. (a) The strider leg and (b) the cockroach leg under an optical Microscope.

From the SEM figures of the strider leg, we can see that there are further patterns on the setae. These patterns also contribute to the hydrophobicity of the leg.

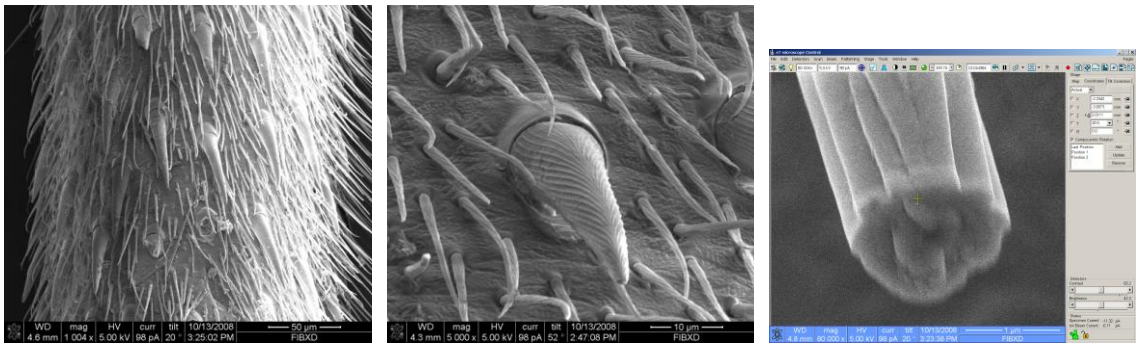

(a.) (b.) (c.)

Figure 12. (a.)The setae on the leg of the strider; (b.)patterns on the big setae; (c.) patterns on the small setae.

5.1.3 The Bio-specimens Modeling with Geometric Shapes

The surfaces of the lotus leaf and the strider leg were simulated with simple geometrical shapes. The angular model was first used, and then developed into the round model. The simulations of the contact angles formed between bio-specimen surfaces and water corresponding to the actual conditions of the real body are compared to the other reported calculations.

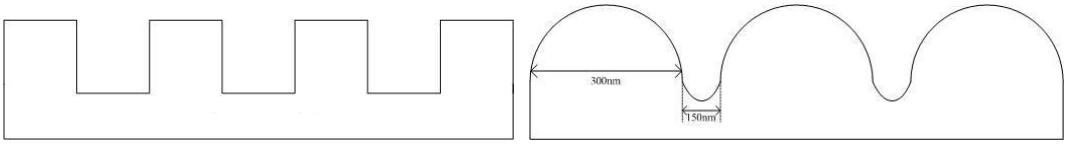

Figure 13. (a,b): Angular and round model simulations.

Using the methods introduced in Sec.3-1-1 and data received from SEM observations, the real contact angle of a single strider setae can be calculated. First the D and F functions that determine the surface roughness, are calculated geometrically. Then, the data is substituted into Eq.(11): $\cos\theta = D(1-F)\cos\theta_0 - F$ to find the real contact. In this case, the original contact angle θ_0 of the material of the strider leg is approximately 105°. The real contact angle θ is calculated to be 123.5°. 125° given behind of this number is referred from the reported study. This is the contact angle of single setae. With numerous setae arranged on the real strider leg, the leg's contact angle can increase up to a value of 170°.

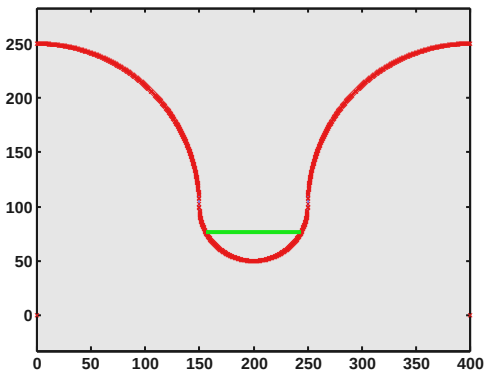

$\theta_0 = 105^\circ$
$D = 1.6426$
$F = 0.221$
$\theta = 123.5^\circ (125^\circ)$

Figure 14. Analysis of single groove of strider leg setae. The part below the red lining is part of the setae surface, and the green line indicates the profile of the stagnant water bridge.

5.2 The Adhesive Forces during Water Treading

5.2.1. Results of the Pilot Study

In order to demonstrate the performance of the system developed in the present study, a pilot study employing a sapphire punch and water drops were designed to measure the results. Figure 15. shows the experimental results of the vertical force.

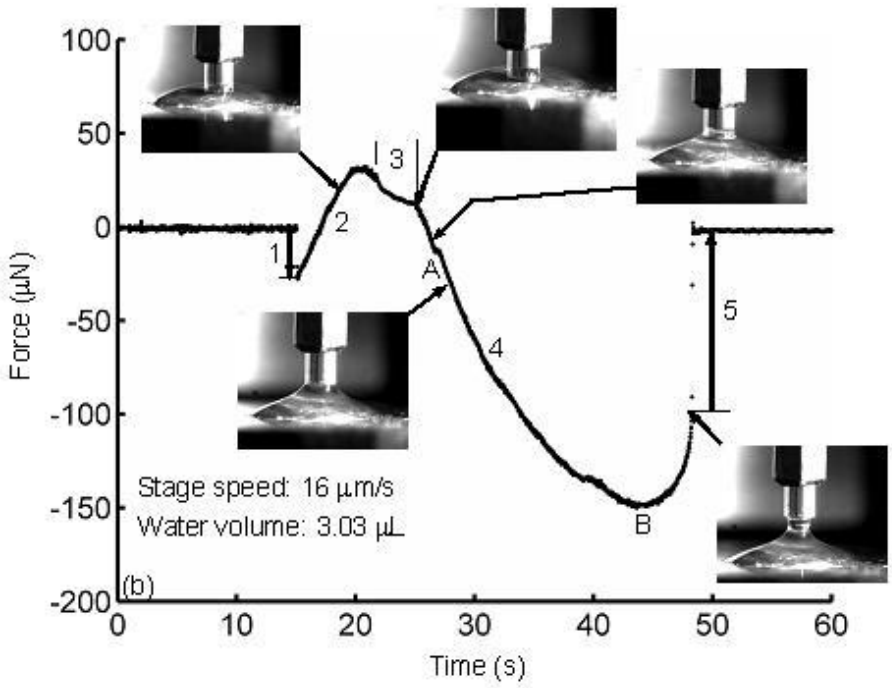

Figure 15. Result for the punch water treading experiment.

Note: 1= jump-into-contact, 2=loading, 3=dwell, 4= unloading, 5= jump-off-contact.

In Figure 15., the positive forces resemble repulsive forces, while the negative forces resemble attractive forces. At the jump-into-contact process, an abrupt attractive force (with negative value) was measured. This is because the distance between the punch and the water droplet got closer, the adhesion of water is allowed to tug at the punch. In the loading process, a repulsive force (with positive

value) was measured. This is because the surface tension of the water droplet was yet broken, and therefore formed the resistance to the punch's entry. In the dwelling process, and the water droplet remained in a certain distance from the punch, the force was seen to drop slightly. During this process the water began to climb up along the lateral surface of the punch due to the capillarity. In the unloading process, an attractive force continued to increase, due to water's adhesion. At the jump-off-contact point the attractive force reduces to zero abruptly.

5.2.2 Forces of the Bio-specimens During Water Treading on Calm Water

The force experiments were conducted for two different biological specimens: the results of the strider leg shown in Figure 16., and the results of the cockroach leg, shown in Figure 17.

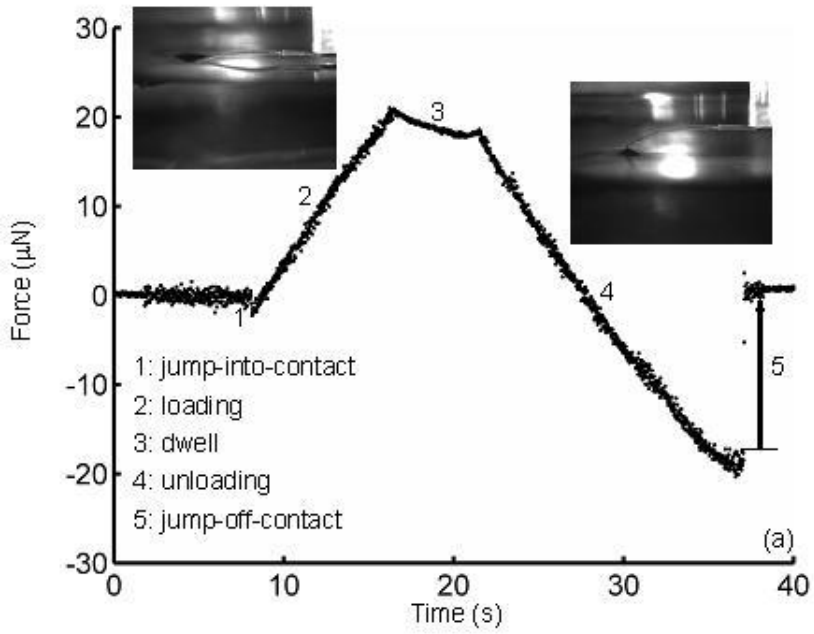

Figure 16. The vertical force results of the strider leg during treading on calm water.

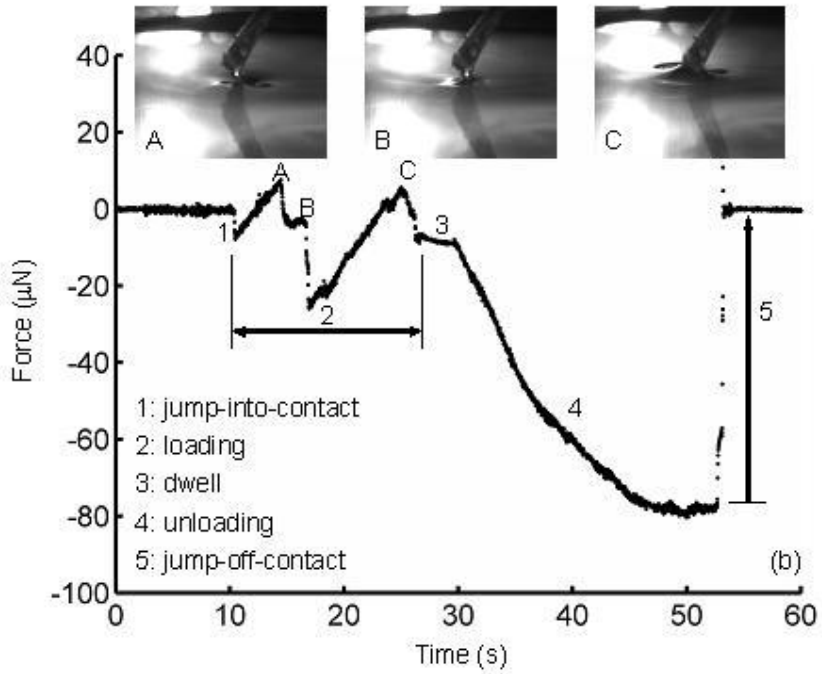

Figure 17. The vertical force results from the cockroach leg during the treading on calm water.

As it is well known, the strider leg is able to float and move swiftly on the water surface while the roach leg sinks soon as it reaches the water. The strider leg surface is paved with dense setae with wax coverings. The roach leg also has setae, however, the spacing between two adjacent setae are much larger than that of the strider. Therefore, the main leg and its setae are easily wetted by water, thus resulting in a higher adhesion.

5.2.3 Vertical Forces of the Strider Leg during Treading on Calm Water

The loading results of the strider leg show the maximum repulsive force of 20 μN, which is 1/5 of the insect's weight. The strider leg gradually depresses the water surface, and an obvious dimple was formed surrounding the treading position. The dimple enlarges as the water surface continues to elevate. According to the theory of floating force, the lift force due to floatation is equal to that of the

weight of the water replaced by the dimple. This explains a bigger dimple provides a higher floating force.

In the dwell process (indicated as process 3 in Figure 16.), the repulsive force is slightly reduced, because the water's adhesion force pulls a small amount of water upward along the leg despite the hydrophobic property of the leg. In the unloading process, the vertical repulsive force is almost linearly decreased with time and the attractive force is linearly increased to about -20 μN at the end of this process. The jump-off-contact force is -20μN, which is approximately the magnitude of the maximum repulsive force. This behavior indicates that the bottom of the leg is hydrophilic, and it has to overcome the adhesion force of water when it needs to leave water, which is larger than the strider's weight.

5.2.4 Vertical Forces of the Roach Leg during Treading on Calm Water

The results of the roach leg show two sections with force increase as well as decrease during the loading process, marked by "1-A", "A-B", "2-C",and"C-3" in Figure 17. In order to investigate the mechanism of force variations, the corresponding images are presented in the same figure. During the two force increasing periods, several dimples were found forming around the treading area; the two maximum repulsive forces resulted from the largest dimples. Then, the dimples suddenly reduce in size and vanish, causing the force to drop. Detailed observations of the roach leg explain the variations of the dimples. As shown in Figure 11.b, the roach leg has thorn-like structures on its surface. Two or three major setae grew downwards (approximately 45° with respect to the side wall of the leg) at every node (see Figure 18.a). These major setae create dimples under a normal critical, as shown schematically in Figure 18., and the dimples continue to

enlarge until the conditions of destroying the dimple are attained. After that, the setae submerge into the water surface and the dimples disappear, thus causing the force to drop.

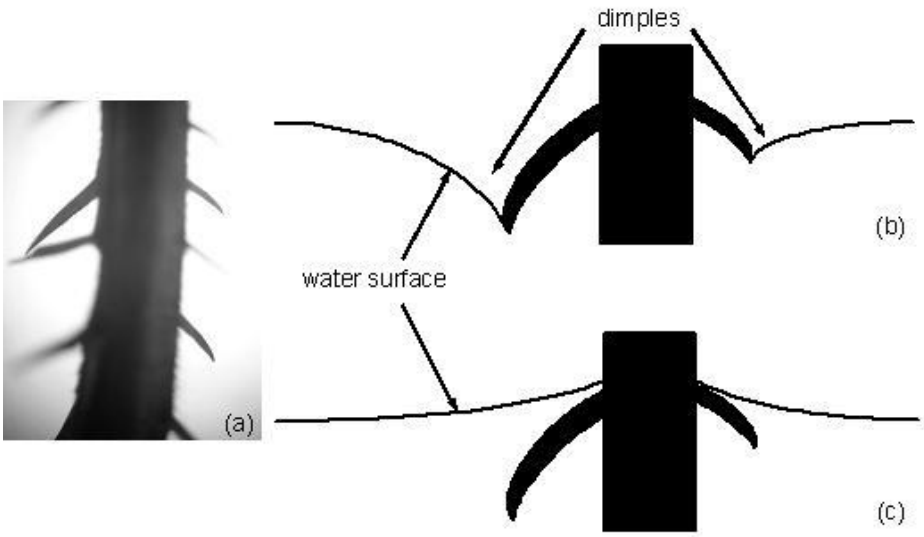

Figure 18. (a) The roach leg and its thorn-like setae; the schematic diagram howing (b) the dimples formed at the thorn end; and (c) the thorns merging beneath the water surface.

Compared to the roach leg, the strider leg produces a larger repulsive force when loading, and receives a smaller attractive force from the water when unloading. This explains how the strider is able to stand on the water while the roach drowns.

5.2.5The Forces during Treading on Vibrating Water

The experiments were conducted with different samples by further vibrating the water vessel horizontally. The vertical force is the force perpendicular to the vibrating direction, while the horizontal force can be measured directly by the transducer (see Figure 19.). We now discuss the differences between results of the strider leg and a fake leg.

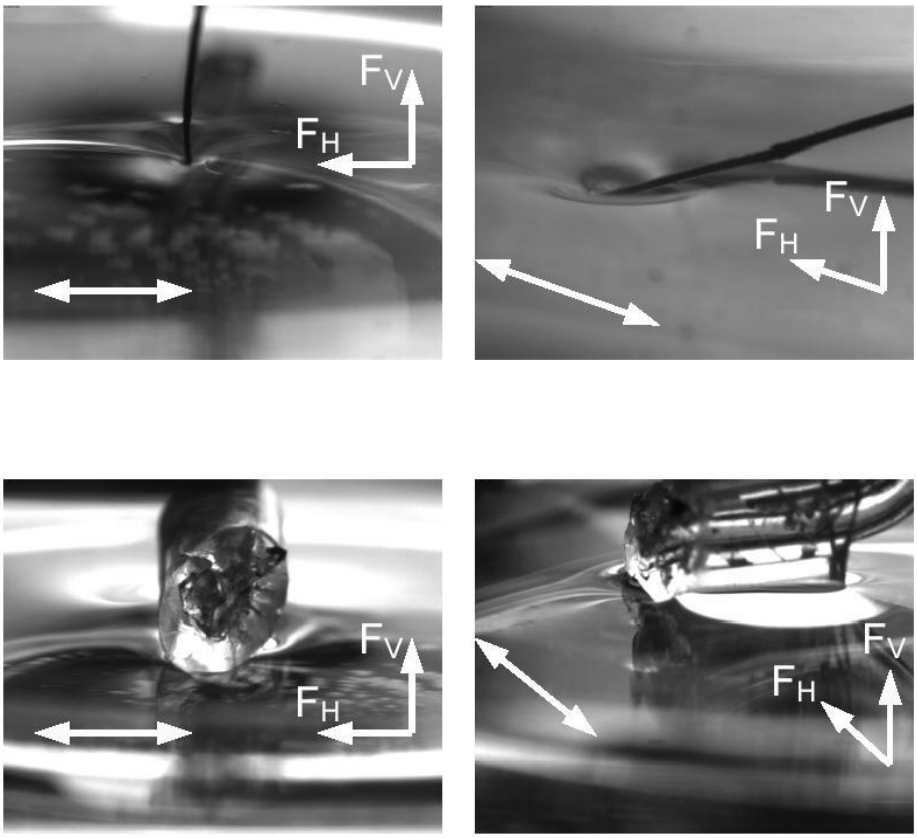

Figure 19. The images of the real leg (top two) and the fake leg (bottom two) While water treading. F_V indicates the measured vertical force; F_H indicates the measured horizontal force. The arrows without force indications are the directions the water vessel is vibrating.

5.2.6 Effect of Vibration

The major factor that affects the measured horizontal and vertical forces is the vertical upheaval of the water that resulted from the vibrations. The undulation is similar to the situation of the strider on a wavy water surface, on which the strider is still able to stand on firmly. We can see from Figure 20. and Figure 21. that the vertical force of the fake leg when vibrated at the frequency of 10 Hz ranges from 40 μN to 160μN, while that of the real strider leg ranges from 10 μN to 40 μN. As for the horizontal force, the fake leg ranges from -50 μN to 50 μN, while the real leg ranges from -10 μN to 10 μN. The maximum vertical force, the maximum horizontal force and the variation rates of the fake leg are all 4-5 times larger than

that of the real leg. In fact, the variation rate of the vertical force of the fake leg shown in Figure 20., Figure 21. is much higher compared to the real leg. The curve slopes of the force-displacement plot shown in Figure 22. represents the effective stiffness. As Figure 22. shows, the stiffness of the true strider leg is much lower than the fake leg's. It reveals the fact that the true strider leg possesses a higher flexibility compared to that of the fake leg, enables the strider to stand firmly on a vibrating water surface.

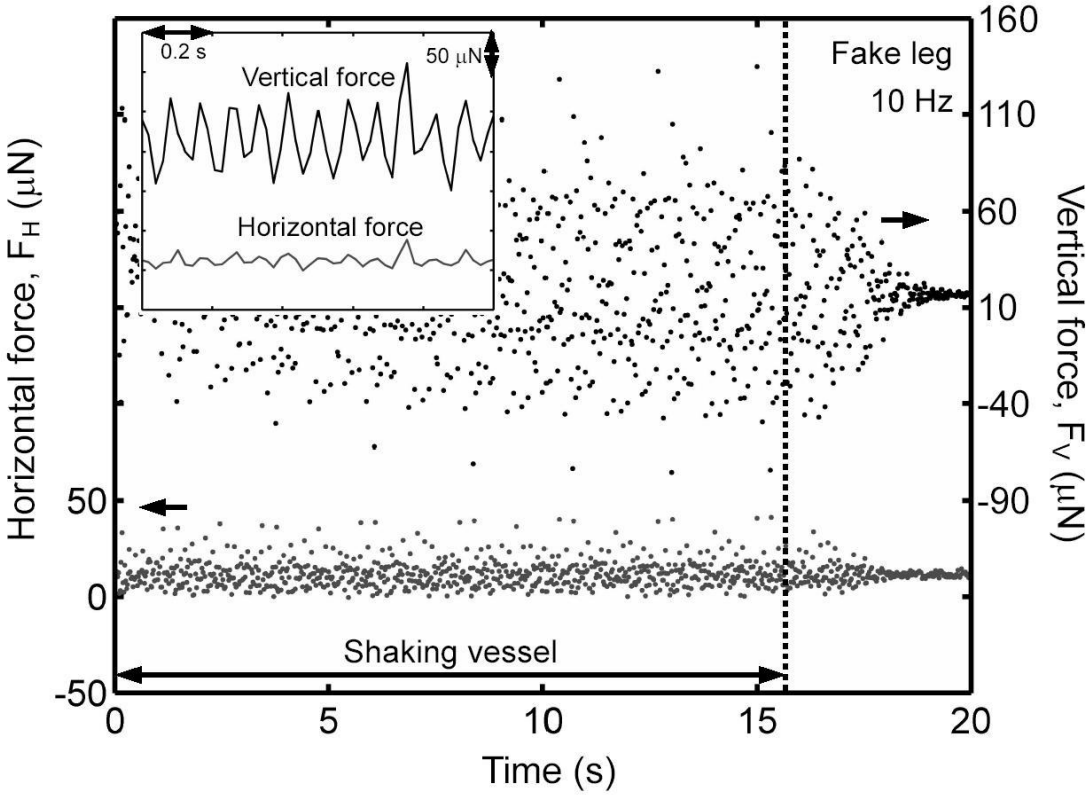

Figure 20. Force results of the fake leg treading in vibrating water.

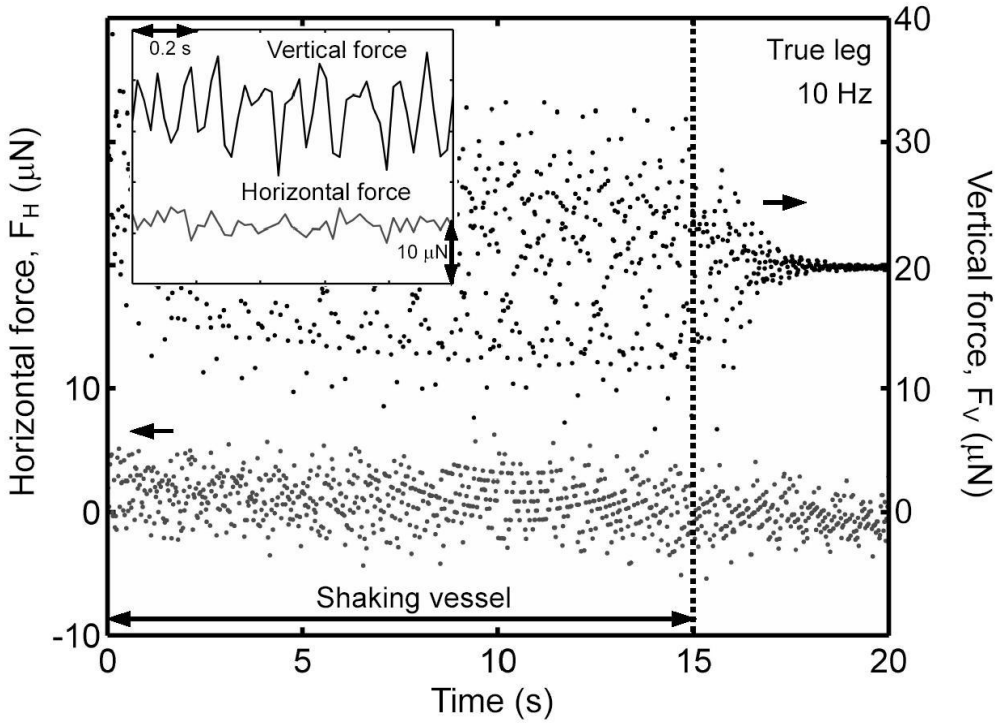

Figure 21. Force results of the real leg water treading in vibrating water.

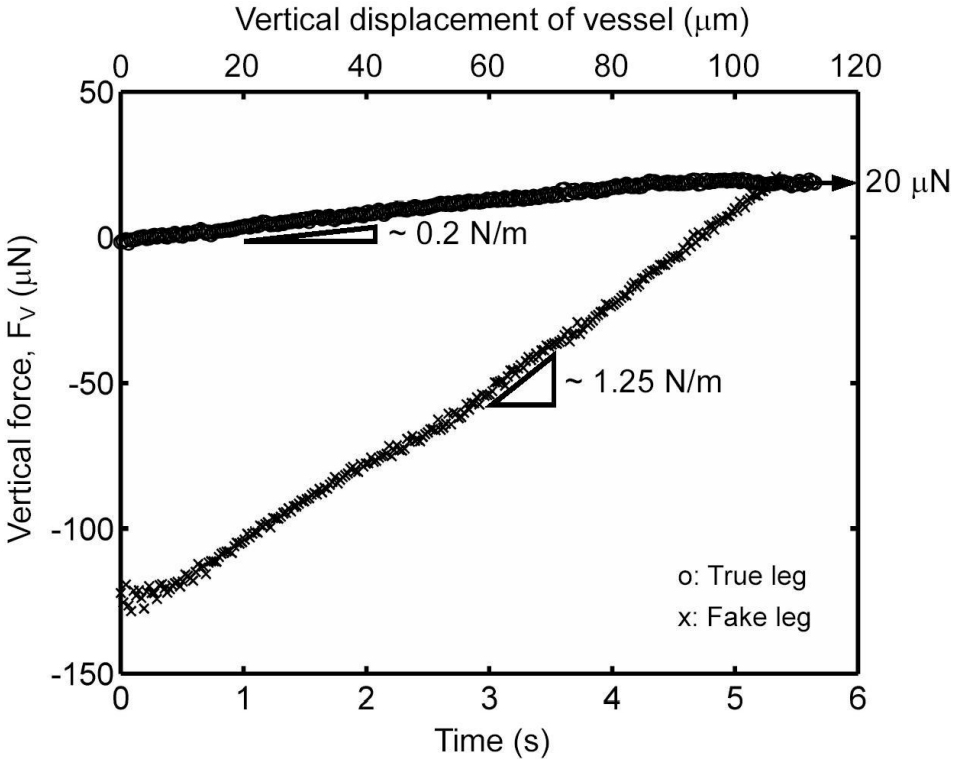

Figure 22. Vertical displacements of the leg and vertical forces as a function of time.

The effective stiffness can be regarded as the anti-vibration behavior demonstrated in a linear spring, as shown in Figure 23. for the fake leg and Figure 24. for the strider leg. The spring responds the attributable to the leg. The small stiffness is partly contributed from the flexibility of a strider leg. For the fake leg, the high effective stiffness in unable to form a dimple despite of the tension (attractive force) or compression (repulsive force) process in the vibrations of water. However, a dimple is easily formed in the strider leg always operating in the compression process. With a small effective stiffness in the strider leg, a small dimple is formed at the beginning of the compression process. However, the dimple is continuously enlarged as compression time is elongated. The significant change in the dimple size is caused due to the high flexibility of the strider leg.

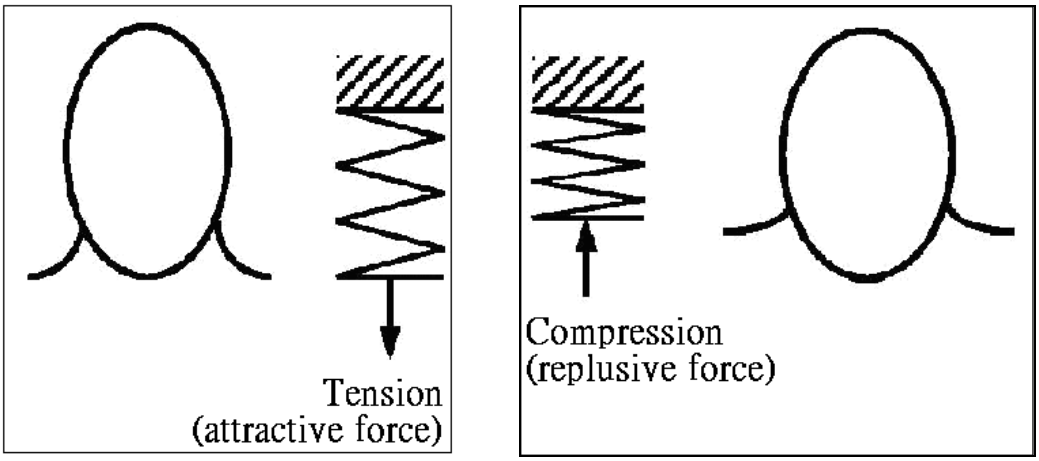

Figure 23. The fake leg regarded as a spring.

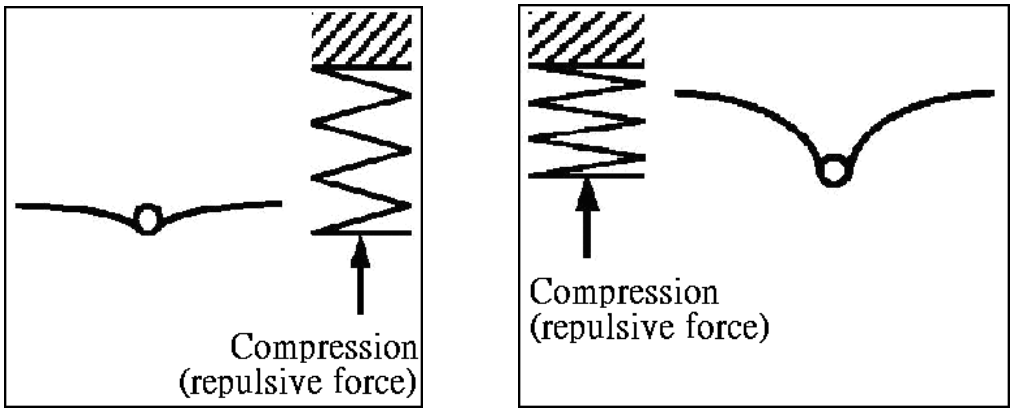

Figure 24. The strider leg regarded as a spring.

The strider leg is like an independent spring mattress (Figure 25.); its legs are like the springs in the mattress, each leg reacts independently to the out-coming force. The strider legs can adjust flexibly when the water surface is undulating, and always maintain the balance of its whole body (Figure 26.).

Figure 25. The strider legs regarded as springs.

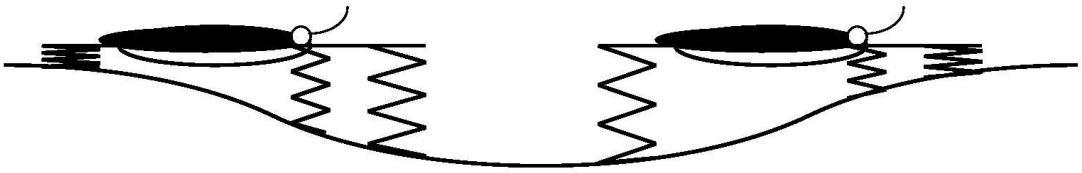

Figure 26. The strider balances on vibrating water surface.

We peel a small part of the real leg off the strider and observe the photograph of the leg using a SEM (see Figure 27.). Besides the setae paved on the outer

surface, the leg is presented to be hollow. This feature not only lessens the weight of the body, and provides more buoyancy, but also allows the leg to be sufficiently more flexible.

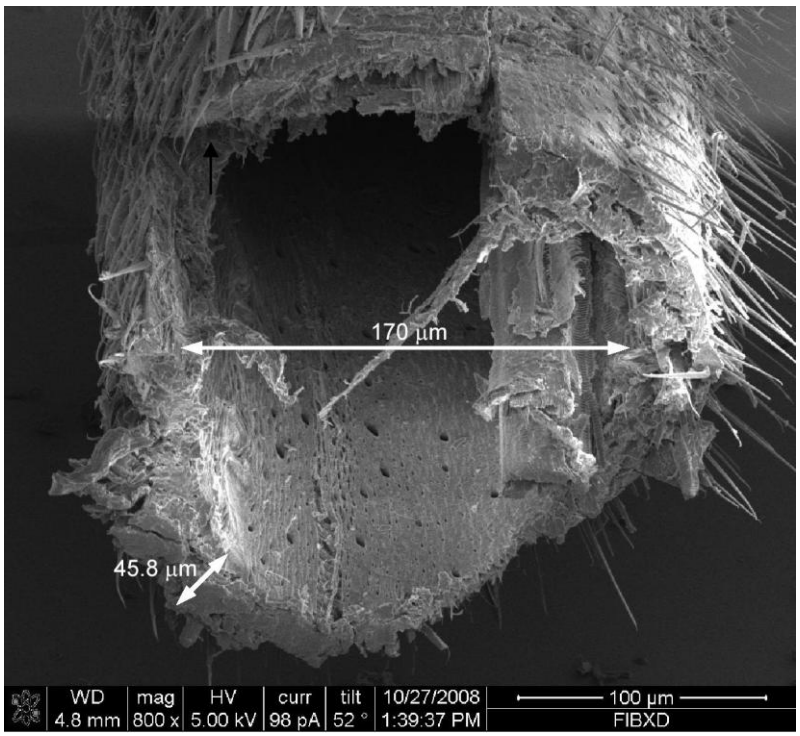

Figure 27. The SEM image for the cross section of the strider leg.

Another important factor that influences the horizontal force is the contact condition of the leg and water. As mentioned in Sec.5.2.2, we know that the strider leg is capable of producing large and stable dimples on the water surface, while the roach leg (and other materials) can only produce small and unstable dimples. These dimples not only affect the buoyancy force of the leg, but also reduce the wetted surface area of the leg and the water. The images of the process also show that the dimple made by the strider leg does not change in size, shape, and depth. It behaves as if the water simply went around the leg and had direct contact at the leg bottom only. Therefore, it was totally not affected by the surrounding water. As shown in Figure 28. we can see that in the dimple, the leg has very little contact

with the water. In fact, the leg only touches the water at the tip, making most of the dimple an aqua-atmosphere interface. This behavior reduces greatly the horizontal force (drag force) due to the viscous effect of water, and makes it easier for the leg to move on the water. However, in the case of the fake leg, the horizontal force is measured several times larger than that of the strider leg. The fake leg does not create a significant dimple in the water; conversely most of the leg surface is covered by water. This allows the water to have a high drag force acting on the leg horizontally, and so the fake leg would need more force to move its legs forward in the water.

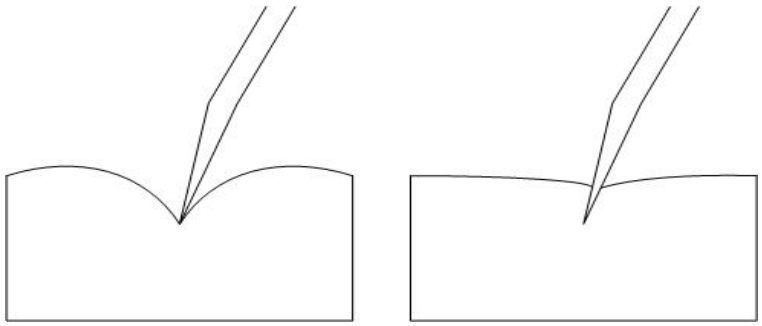

Figure 28. The water surfaces profile created when the strider leg (left) and the roach leg (right) approach.

Observing the process of the vibrating, the relationship between the wettability and contact angle and drag force can be confirmed. Shown in Figure 29. is the process of the vibration. At first, when the water was calm, the strider leg creates a great dimple on the water and maintains a contact angle bigger than 165 degrees (Figure 29.a). When the water starts to vibrate, the water is pushed toward the leg one side at a time (Figure 29.b and Figure 29.c). The force of the moving water pressures the water into the grooves of the strider leg (Figure 29.f). As we know from our equation before, the amount of water in the grooves of the material highly affects the contact angle. The contact angle at the side where the water is

pushed at decreases to 67 degrees, while the other side remains the same Figure 29.e). As the water is vibrated, the water rushes at both sides of the leg in turn. after three cycles, the dimple decreases and the leg sinks deeper into the water, and the contact angle decreases (Figure 29.d).

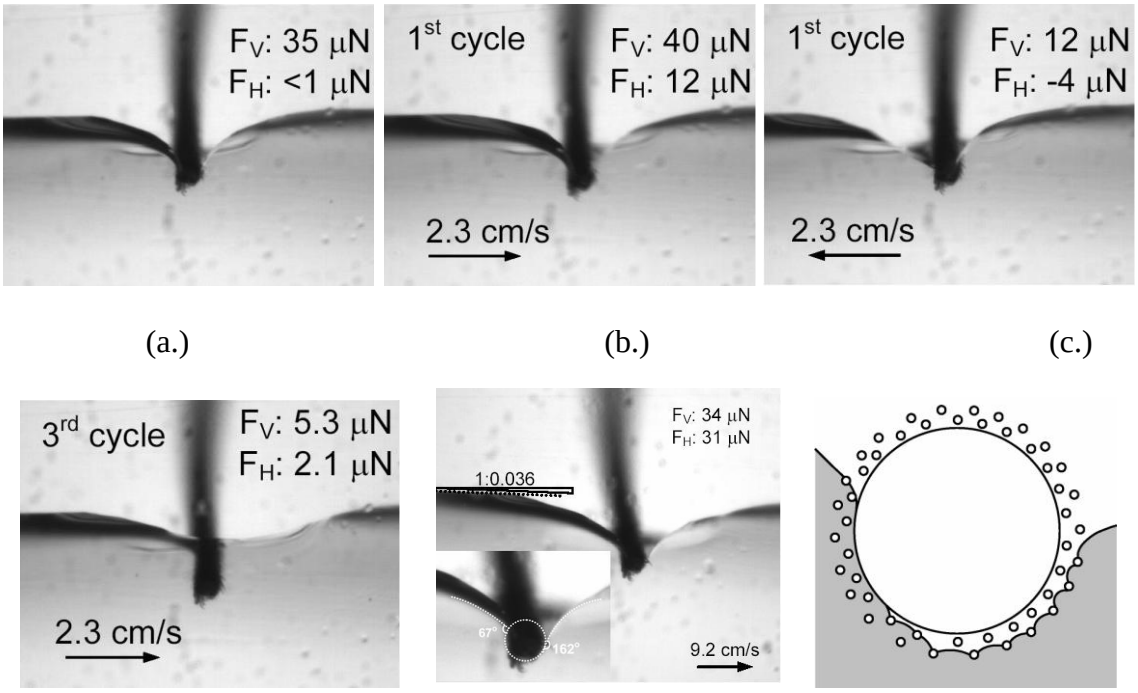

Figure 29. Process of the vibration.

5.2.7 Forces Produce during Treading on Flowing Water

The water treading experiments were carried out at an uniform flow with a strider leg and a fake leg. The vertical force is controlled at 20 μN, while the water surface was maintained to be smooth as possible as we can. The force results of both legs are shown in Figure 30. and Figure 31.

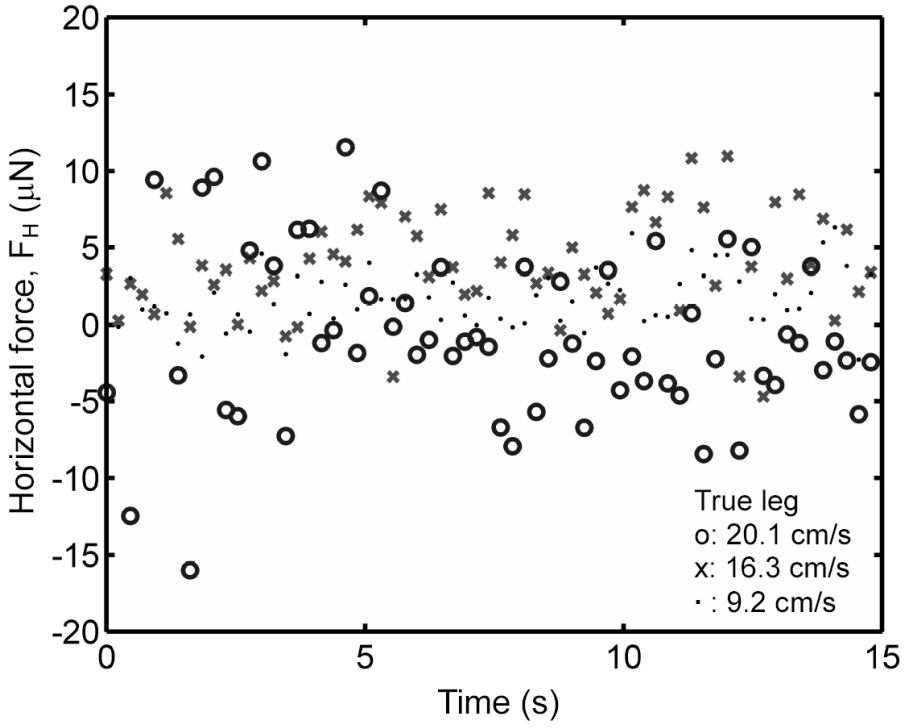

Figure 30. Force results of the true leg water treading against uniform flows of different velocity.

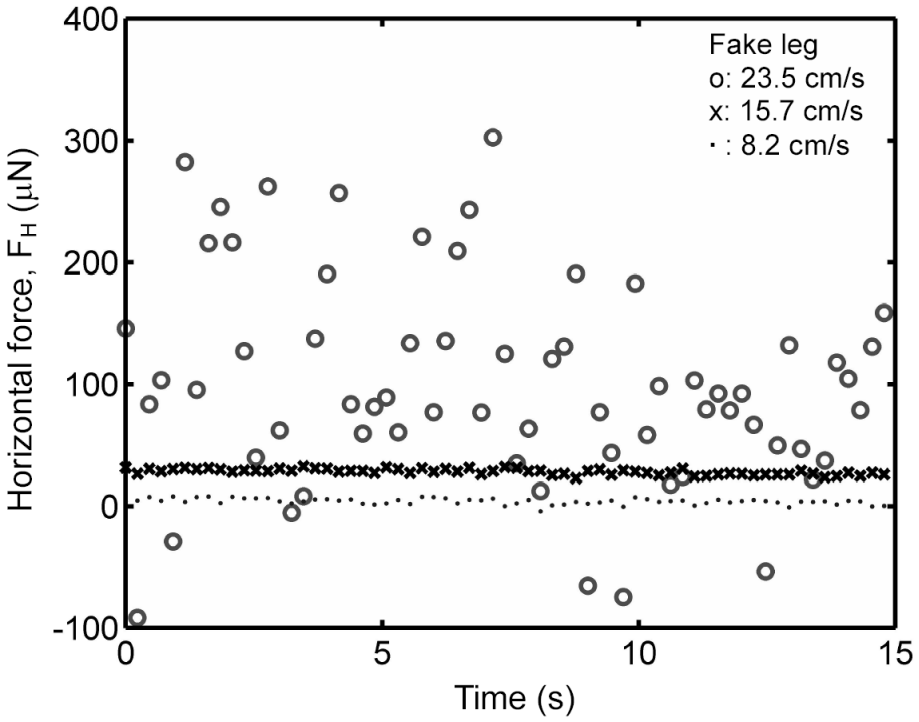

Figure 31. Force results of the fake leg water treading against uniform flows of different velocity.

5.2.8 Force Results

In Figure 30., the horizontal force measured of the true leg ranges from -15 μN to 20 μN. The force ranges vary while treading in uniform flows at different velocities. Evidentally, the faster the water flows, the greater the variation of the measured forces. However, the force is seen to be in a wide range of -15 μN to 20 μN. The difference among the three mean force results corresponding three flow velocities are considerably small; in fact they are varied almost on the noise level of the indenter. The variations of the horizontal force results of the fake leg are also larger (see Figure 31.). However, the range of the force variations becomes small at the low velocities (8.2 cm/s and 15.7cm/s). The force is increased by increasing the flow velocity if the fake leg was tested. The force variations ranging from -100 μN to 300 μN, is more than 10 times of the range of the real leg.

For the fake leg, the Reynolds number $Re = V D / \nu$ varies from 100 to 200(laminar flow), where V = 20 ~ 10 cm/s denotes the mean flow velocity and D = 1 mm denotes the characteristic diameter of the glass tube. ν represents the kinetic viscosity of water The drag coefficient $C_D = F_H / (\rho V^2 A /2)$ varied from 1.5 to 0.6 as A = 5 mm^2 is the frontal area against the uniform flow, which is reasonable for a cylinder.

The drag force of the real leg is much smaller compared to the fake leg due to the leg's hydrophobicity. According to the theory of fluid dynamics, the drag force consists of friction force and pressure force. The diameter of the true leg was measured to be about 0.2mm, the depth beneath the water surface is about 1/5 of the entire leg, as shown in Figure 31. For the same buoyancy force, the frontal area of the real leg is much smaller than the fake leg, thus resulting in a smaller pressure

force. However, the pressure force is only responsible for a small part of the drag force, itm is a miner factor as to the drag force. The true leg is not completely wetted; the wetted area (solid-fluid interface) fraction of setae with respect to the outer surface is around 0.05-0.1. The friction between the true leg and the water is expected to be low because of the small wetted area fraction of the solid-fluid interface.

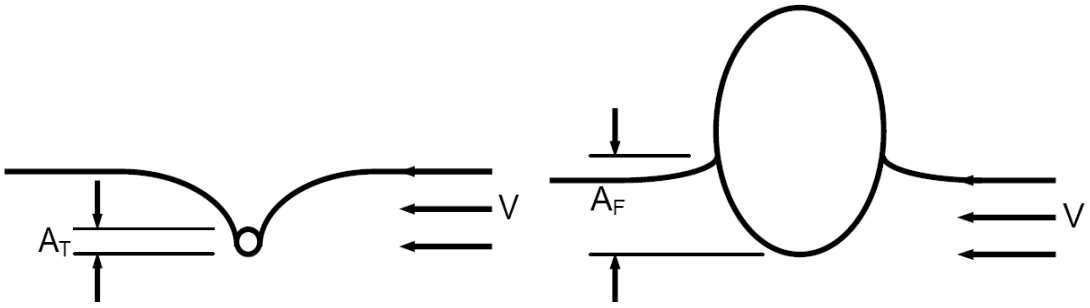

Figure 32. The profiles of water surfaces created by placing the true leg (left) and the fake leg (right) in uniform flow.

6. Conclusions

In the theoretical part of this study, the present method can be used to find the water bridge profile and the stagnant point of the water bridge on the lateral surface of a groove if the groove geometry and the hydrophobicity of the groove surface are given. The water bridge profile can be applied to determined the real contact angle (θ) corresponding to an initial contact angle (θ_0). In the completely un-wetted state, $D = F = 1$. In the transitional region between the fully wetted state and un-wetted state, the D parameter nonlinearly decreases with increasing θ_0 value while the F parameter nonlinearly increases with increasing θ_0 value. Irrespective of the asperity aspect ratio, the θ angle in the fully wetted and transitional regions is increased by increasing the θ_0 angle. The present method is used on simulating models of the lotus

leaf and strider leg to understand the hydrophobicity of the two materials.

From our experimental studies, the forces of the strider leg treading on calm, vibrating, and running waters is measured with a self-developed system. Treading on calm water, the repulsive force and adhesion measured are both approximately 20 μN, which explains the buoyancy caused by the dimple created by the strider leg. The repulsive force results from the hydrophobicity of the strider leg, which can be indicated by the large contact angle of the leg. When treading in vibrating and running waters, the horizontal forces measured are both between -10 μN and 10 μN, while the vertical forces measured are between 10-40 μN, which are so small that they are close to the noise level of the indenter. This indicates that the strider leg has great antivibration and antifriction abilities, which help the insect remain steady on the water surface. The measured force is believed to be minimal because of the small contact area ratio of the liquid-solid interface, that is, the hydrophobicity of the leg. The hydrophobicity of the leg is caused by the formation of numerous setae on the leg. The setae itself is highly hydrophobic in structure, and is analyzed by the newly developed theoretical method. The contact angle of a setae is calculated to be 123.5°. The combination of many setae results in a contact angle of over 170°on water for the strider leg, which indicates the hydrophobicity of the strider leg. Also, from our observations of the strider leg treading on moving water, the wettability of the material can affect the contact angle and drag force of the material. These can confirm the correctness of our equation.

7. References

1. Bush, J. W. M.; Prakash, M.; Hu, D. L. AdV. Insect Physiol. (2008), 34 117.
2. Cassie A. B. D. and Baxter S., (1944) Trans. Faraday Soc. 40 546.
3. Feng X. Q., Gao X., Wu Z., Jiang L., and Zheng Q. S., (2007) Langmuir 23 4892.
4. Wenzel, R. N. (1936) Ind. Eng. Chem. 28 988.
5. Zhou X. B. and Hosson J. T. M. D., (1995) J. Mater. Res. 10 1984.
6. Hung, C.K. and Huang, C.M. The Morphological Character of Lotus Foliage and its Effect on the Self-cleaning Property. (2008)

Acknowledgments: This work was supported by the Center for Frontier Materials and Micro/Nano Science and Technology Center, National Cheng Kung University, Taiwan.

評語

實驗上很精確量測水黽腳垂直及平行於水面之各項作用力之值，同時亦有一組人造腳之對照數據。

兩人合作無間，呈現對主題特性均有一定程度的瞭解。

然作用力不只是與形狀有關，也與材質有關，而這部分之探討較缺乏。